J. Fluid Mech. (2020), *vol*. 900, R3, doi:10.1017/jfm.2020.543



Parametrically forced stably stratified flow in a three-dimensional rectangular container

Jason Yalim[1], **Juan M. Lopez**[1,†] **and Bruno D. Welfert**[1]

[1]School of Mathematical and Statistical Sciences, Arizona State University, Tempe, AZ 85287, USA

(Received 28 March 2020; revised 27 June 2020; accepted 30 June 2020)

The dynamics of a stably and thermally stratified fluid-filled cavity harmonically forced in the vertical direction, resulting in a periodic gravity modulation, is studied numerically. Prior simulations in a two-dimensional cavity showed a myriad of complex dynamic behaviours near the onset of instabilities, and here we address the extent to which these persist in three dimensions. Focusing on a parameter regime where the primary subharmonic mode is resonantly driven, we demonstrate comprehensive qualitative agreement between the dynamics in two and three dimensions; the quantitative difference is due to the larger forcing amplitudes needed in three dimensions to overcome the additional viscous damping from the spanwise walls. Using a small detuning of the forcing frequency, together with a relatively large forcing amplitude, leads to a wave-breaking regime where the qualitative agreement between two and three dimensions breaks down.

Key words: internal waves, parametric instability

1. Introduction

Parametrically driven instabilities in continuously stratified flows have drawn much attention due to their potential importance in dynamical processes in the ocean and atmosphere. They have been extensively studied at a fundamental level in laboratory experiments (e.g. Thorpe 1968; McEwan 1971; McEwan & Robinson 1975; Bouruet-Aubertot, Sommeria & Staquet 1995; Benielli & Sommeria 1998; Staquet & Sommeria 2002; Joubaud *et al.* 2012; Sutherland 2013; Dauxois *et al.* 2018). The experiment of Benielli & Sommeria (1998), where a rectangular cavity filled with a uniformly stratified solution of brine was oscillated vertically, is a particularly clean set-up. With the forcing being due to a modulation of the effective gravity, the state of zero relative velocity with linear stratification loses stability when the secular growth of a parametrically forced standing internal wave mode is faster than the rate at which it dissipates viscously. In contrast, when the system is forced by oscillating plungers

† Email address for correspondence: juan.m.lopez@asu.edu

© The Author(s), 2020. Published by Cambridge University Press

https://doi.org/10.1017/jfm.2020.543 Published online by Cambridge University Press

or paddles (Thorpe 1968; McEwan 1971), the static stratified state is not a solution as wave beams from the oscillating plungers and paddles are always generated, complicating the analysis of the response flow. Nevertheless, Thorpe (1968) was able to interpret his experimental results in terms of two-dimensional (2-D) intrinsic standing wave modes of the inviscid 2-D rectangular cavity. This was possible so long as the plunger amplitude was not too large, so that the response flow (or at least the density variations) remained invariant in the spanwise direction. McEwan (1971) also noted that the flow remained 2-D for paddle oscillation amplitudes that were not too large.

The experiments of Benielli & Sommeria (1998) using modulation of the effective gravity were conducted in a container with an approximately square cross-section (26.1 cm wide and filled to a height of 25 cm) and a span of 9.6 cm. Only the 2-D modes were resonantly excited by the forcing in parameter regimes near the centre of their resonant tongues; the short span width resulted in the three-dimensional (3-D) modes that could fit in the container being viscously damped. This motivated our prior 2-D studies using a square container with gravity modulation. In Yalim, Lopez & Welfert (2018), the linear stability of the forced viscous problem, using temperature stratification, was determined via Floquet analysis over a large range of buoyancy-to-viscous time-scale ratios and forcing amplitudes and frequencies. Temperature rather than salt was used for stratification, as the fixed temperature boundary conditions on the top and bottom endwalls result in the state of zero relative velocity and stable linear temperature stratification being an equilibrium solution that exists for all parameter values. The Floquet analysis determined the stability of this equilibrium. Those results were used to develop a reduced model to quickly determine instability regimes (Yalim, Welfert & Lopez 2019*a*). The Floquet analysis, however, does not provide any indication as to what the response flow is when the equilibrium is unstable. Yalim, Welfert & Lopez (2019*b*) addressed this by studying the fully nonlinear 2-D problem, uncovering a wealth of complex dynamics. Restricting the simulations to two dimensions allowed for a very detailed exploration of the nonlinear dynamics, particularly near the tip and centre of the broadest resonance tongue, the subharmonic $1:1$ tongue. The observed dynamics involved a symmetry-breaking flip bifurcation, which was either supercritical to the high-frequency side of the tip of the tongue or subcritical to the low-frequency side, resulting in a subharmonic limit cycle $\mathrm{L}_{1:1}$. This limit cycle undergoes both pitchfork and Neimark–Sacker bifurcations, resulting in symmetry conjugate limit cycles and quasi-periodic 2-tori in different parts of the tip. All of these states undergo secondary bifurcations, resulting in a multiplicity of unstable saddle states. Gluing bifurcations and various heteroclinic cycles, including a complex homoclinic-doubling sequence which has some similarities to the dynamics of the logistic map, were found.

A primary goal of the present study is to determine to what extent the 2-D results (Yalim *et al.* 2019*b*) persist in three dimensions. To this end, we study the nonlinear dynamics in a container with a square cross-section and a spanwise aspect ratio corresponding to that of the container used in the experiments of Benielli & Sommeria (1998). This is done via numerical simulations of the 3-D Navier–Stokes equations using the Boussinesq approximation and thermal stratification.

2. Governing equations, symmetries and numerics

Consider a fluid of kinematic viscosity ν, thermal diffusivity κ and coefficient of volume expansion β contained in a cavity of square cross-section with sides of length L and

https://doi.org/10.1017/jfm.2020.543 Published online by Cambridge University Press

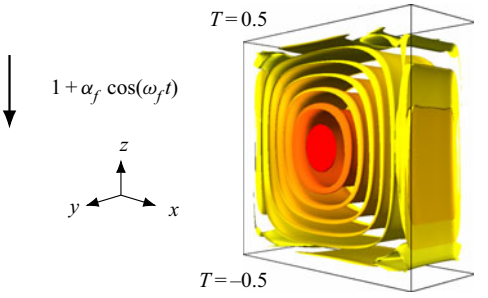


FIGURE 1. Schematic of the vertically oscillating cavity. The perspective is of the clipped (boundary layers removed) spanwise vorticity ω_y for an $L_{1:0:1}$ response at $Rn = 2 \times 10^4$, $\alpha_f = 0.15$ and $\omega_f = 1.41$.

spanwise width W. The four sidewalls are thermally insulated, whereas the top and bottom endwalls are held at constant temperatures, with the temperature difference between the top and bottom walls $\Delta T = T_T - T_B > 0$. Gravity g is aligned in the downward vertical direction. In the absence of any other external force, the fluid is linearly stratified and at rest. The system is non-dimensionalized using L as the length scale and $1/N$ as the time scale, where $N = \sqrt{g\beta\Delta T/L}$ is the buoyancy frequency. The non-dimensional temperature is $T = (T^* - T_B)/\Delta T - 0.5$. A Cartesian coordinate system fixed to the cavity is used with its origin at the centre of the cavity; z is the vertical direction and y is the spanwise direction, such that $\boldsymbol{x} = (x, y, z) \in [-0.5, 0.5] \times [-W/2L, W/2L] \times [-0.5, 0.5]$. The velocity is $\boldsymbol{u} = (u, v, w)$ and the vorticity is $\boldsymbol{\omega} = \boldsymbol{\nabla} \cdot \boldsymbol{u} = (\omega_x, \omega_y, \omega_z)$. The cavity is subjected to harmonic oscillations in the vertical direction of angular frequency f and vertical displacement ℓ. Figure 1 is a schematic of the set-up.

Under the Boussinesq approximation, the non-dimensional governing equations in the cavity frame are

$$\left.\begin{gathered} \partial \boldsymbol{u}/\partial t + \boldsymbol{u} \cdot \boldsymbol{\nabla} \boldsymbol{u} = -\boldsymbol{\nabla} p + Rn^{-1} \nabla^2 \boldsymbol{u} + (1 + \alpha_f \cos \omega_f t) T \boldsymbol{e}_z, \quad \boldsymbol{\nabla} \cdot \boldsymbol{u} = 0, \\ \partial T/\partial t + \boldsymbol{u} \cdot \boldsymbol{\nabla} T = (Pr\, Rn)^{-1} \nabla^2 T, \end{gathered}\right\} \tag{2.1}$$

where p is the reduced pressure. There are five non-dimensional parameters:

$$\left.\begin{array}{cc} \text{buoyancy number} & Rn = NL^2/\nu, \\ \text{Prandtl number} & Pr = \nu/\kappa, \\ \text{spanwise aspect ratio} & \gamma = W/L, \\ \text{forcing frequency} & \omega_f = f/N, \\ \text{forcing amplitude} & \alpha_f = f^2 \ell/g. \end{array}\right\} \tag{2.2}$$

The no-slip boundary condition in the cavity frame is $\boldsymbol{u} = \boldsymbol{0}$ on all six walls. The temperature boundary conditions are $T_x(\pm 0.5, y, z) = T_y(x, \pm 0.5\gamma, z) = 0$ and $T(x, y, \pm 0.5) = \pm 0.5$. The governing equations and boundary conditions are equivariant to reflections about the three midplanes, $\mathcal{K}_x$, $\mathcal{K}_y$ and $\mathcal{K}_z$. Their composition is a reflection through the origin, known as a centrosymmetry, whose action is

$$\mathcal{C} : [u, v, w, T](x, y, z, t) \mapsto [-u, -v, -w, -T](-x, -y, -z, t). \tag{2.3}$$

https://doi.org/10.1017/jfm.2020.543 Published online by Cambridge University Press

Owing to the periodic forcing, the system is also invariant to a time translation,

$$\mathcal{P}_\tau : [u, v, w, T](x, y, z, t) \mapsto [u, v, w, T](x, y, z, t + \tau), \tag{2.4}$$

where $\tau = 2\pi/\omega_f$ is the forcing period. The basic state,

$$\boldsymbol{u}_b = \boldsymbol{0}, \quad T_b = z \quad \text{and} \quad p_b = 0.5z^2(1 + \alpha_f \cos \omega_f t), \tag{2.5a–c}$$

is both $\mathcal{C}$ and $\mathcal{P}_\tau$ invariant. It exists for all values of the governing parameters, but loses stability as these are increased above critical levels. Instabilities are typically associated with symmetry breaking.

Linearizing (2.1) about the basic state (2.5*a–c*), neglecting thermal and viscous diffusion (taking $Rn \to \infty$), and in the absence of gravitational modulations ($\alpha_f = 0$), leads to an eigenvalue problem for the inviscid intrinsic modes of the stratified cavity. These modes are periodic in all three directions, satisfy no-penetration boundary conditions and can be obtained via separation of variables. They vary harmonically in time with frequency $\sigma_{m:k:n} \in (0, 1)$, given in terms of integer half-wavenumbers m, k and n in the x, y and z directions by the dispersion relation

$$\sigma^2_{m:k:n} = \frac{m^2 + (k/\gamma)^2}{m^2 + (k/\gamma)^2 + n^2}. \tag{2.6}$$

The spatial harmonics all have the same temporal frequency, $\sigma^2_{m:k:n} = \sigma^2_{jm:jk:jn}$ for any positive integer j. When $k = 0$ or $\gamma \to \infty$, the modes reduce to the 2-D eigenmodes determined by Thorpe (1968), with $v = 0$ and independent of y.

Space is discretized via spectral collocation with Chebyshev polynomials of degree n_c in barycentric form, and time evolution uses the fractional-step improved projection scheme of Mercader, Batiste & Alonso (2010). We have implemented this method previously in related problems (Lopez *et al.* 2017; Wu, Welfert & Lopez 2018; Yalim *et al.* 2018, 2019*b*). Most of the results presented in this study were obtained with Chebyshev polynomials of degree $n_c = 48$ in the x, y, and z directions and up to 200 time steps per forcing period. Converged quasi-periodic flows were run for at least 50 000 forcing periods. Flows driven by large-amplitude forcing with wave breaking require much greater spatio-temporal resolution; for these cases $n_c = 384$ and 4000 time steps per forcing period were used.

The flows are visualized using isotherms and spanwise vorticity contours at the spanwise midplane in order to allow for direct comparisons between 2-D and 3-D solutions, and

$$Q_N = \frac{\|\boldsymbol{R}\|^2 - \|\boldsymbol{S}\|^2}{\|\boldsymbol{R}\|^2 + \|\boldsymbol{S}\|^2} = \frac{|\boldsymbol{\omega}|^2 - \Phi}{|\boldsymbol{\omega}|^2 + \Phi}, \quad Q_N \in [-1, 1], \tag{2.7a,b}$$

where $\boldsymbol{R} = (\boldsymbol{J} - \boldsymbol{J}^{\mathrm{T}})/2$ is the rate-of-rotation tensor and $\boldsymbol{S} = (\boldsymbol{J} + \boldsymbol{J}^{\mathrm{T}})/2$ is the rate-of-strain tensor, which are respectively the skew-symmetric and symmetric components of the velocity gradient tensor $\boldsymbol{J} = \nabla \boldsymbol{u}$, $\Phi = 2\|\boldsymbol{S}\|^2$ is the viscous dissipation and $\|\cdot\|$ denotes the Frobenius norm. For incompressible flows, $Q_N = 2Q/\|\boldsymbol{J}\|^2$ is a normalization of the Q-criterion of Hunt, Wray & Moin (1988), measuring the relative strengths of $\boldsymbol{R}$ and $\boldsymbol{S}$. On no-slip boundaries $Q_N = 0$, and regions in space with $Q_N > 0$ are where $\boldsymbol{R}$ dominates over $\boldsymbol{S}$. The isosurface level $Q_N = 0.04$ (corresponding to level $(1 + Q_N)/2 = 0.52$ of the related Ω-criterion of Liu *et al.* (2016)) provides a remarkably good visualization of the flow's vortex structure in three dimensions.

https://doi.org/10.1017/jfm.2020.543 Published online by Cambridge University Press

3. Dynamics in the 1 : 0 : 1 subharmonic resonance tongue

Benielli & Sommeria (1998) experimentally investigated the responses in a short spanwise cavity ($\gamma \approx 0.4$) at forcing frequency $\omega_f \approx 2/\sqrt{2}$, corresponding to the middle of the 1 : 0 : 1 subharmonic resonance tongue (the natural frequency of the 1 : 0 : 1 intrinsic mode is $\sigma_{1:0:1} = 1/\sqrt{2}$). They had $Rn \approx 1.2 \times 10^5$ ($N = 1.96$ s^{-1}, $L = 25$ cm, $\nu = 0.01$ cm^2 s^{-1}) and a Schmidt number of order 700 (corresponding to salt in water), which are quite challenging for an extensive numerical parametric study, even in two dimensions. In our 2-D numerical study (Yalim *et al.* 2019*b*), we used $Rn = 2 \times 10^4$ and $Pr = 1$ for an extensive study in the forcing frequency and amplitude, considering $\omega_f \in (0, 2.5)$ and $\alpha_f \in (0, 1)$. In the present 3-D numerical study, we use the same geometry as Benielli & Sommeria (1998), with $\gamma = 0.4$, and also consider the response in the 1 : 0 : 1 subharmonic resonance tongue, with $\omega_f = 1.41 \approx 2/\sqrt{2}$ and $\alpha_f \in (0, 0.3]$. We keep $Rn = 2 \times 10^4$ and $Pr = 1$ as in the 2-D study in order to make direct comparisons between the response flows in the two studies.

Figure 2 presents bifurcation diagrams from simulations in two dimensions (reproduced from Yalim *et al.* (2019*b*)) and in three dimensions with $\gamma = 0.4$, both at $Rn = 2 \times 10^4$, $Pr = 1$ and $\omega_f = 1.41$. The state measure in both is the variance in the u velocity at a point, Σ^2_{2D} and Σ^2_{3D}. The point in two dimensions is $(x, z) = (1/\sqrt{8}, 1/\sqrt{8})$ and in three dimensions it is at the corresponding point on the spanwise midplane $(x, y, z) = (1/\sqrt{8}, 0, 1/\sqrt{8})$. The two bifurcation diagrams are qualitatively similar; the basic state (2.5*a–c*) loses stability to a limit cycle whose period is twice that of the forcing period; its spatial structure matches that of the 1 : 1 mode in two dimensions and the 1 : 0 : 1 mode in three dimensions, and the intrinsic frequencies of the modes are $\sigma_{1:1} = \sigma_{1:0:1} = 1/\sqrt{2} \approx 0.5\omega_f$. The critical forcing amplitudes at onset of instability differ: $\alpha_f \approx 0.066$ in two dimensions versus $\alpha_f \approx 0.143$ in three dimensions. The larger forcing in three dimensions is needed to overcome the viscous damping from the spanwise walls at $y = \pm 0.5$. A snapshot of the spanwise vorticity ω_y at forcing phase $\pi/2$ and the isotherms at forcing phase $3\pi/2$ of the 2-D limit cycle $\mathrm{L}_{1:1}$ and that of the 3-D limit cycle $\mathrm{L}_{1:0:1}$ in the spanwise midplane $y = 0$ are shown in the first column of figure 3. The states are a little beyond onset, at $\alpha_f = 0.07$ for the 2-D and $\alpha_f = 0.15$ for the 3-D cases. They are very similar. At the subharmonic bifurcation, both the centrosymmetry $\mathcal{C}$ and the τ periodicity $\mathcal{P}_\tau$ are broken; however, the cycles retain a spatio-temporal symmetry consisting of the composition $\mathcal{C}\mathcal{P}_\tau$ (a half-period-flip symmetry). Furthermore, $\mathcal{P}_\tau$ conjugates are also spawned, $\mathcal{P}_\tau(\mathrm{L}_{1:1})$ in two dimensions and $\mathcal{P}_\tau(\mathrm{L}_{1:0:1})$ in three dimensions. All have invariance to the combined reflections in x and z, $\mathcal{K}_x\mathcal{K}_z$ (but not to just one or the other reflection), and $\mathrm{L}_{1:0:1}$ is also spanwise reflection $\mathcal{K}_y$ invariant.

The limit cycles undergo a pitchfork bifurcation, at $\alpha_f \approx 0.101$ in two dimensions and $\alpha_f \approx 0.167$ in three dimensions, breaking the half-period-flip symmetry $\mathcal{C}\mathcal{P}_\tau$ and spawning two subharmonic limit cycles, LL_{2D} and LR_{2D} in two dimensions and LL_{3D} and LR_{3D} in three dimensions (along with their $\mathcal{P}_\tau$ conjugates). These states are symmetrically related by a reflection either in x or in z: $\mathcal{K}_x\,\mathrm{LL} = \mathrm{LR}$ and $\mathcal{K}_z\,\mathrm{LL} = \mathrm{LR}$, in both two and three dimensions. The second and third columns of figure 3 show snapshots of these. The fourth column of figure 3 shows snapshots of another limit cycle, $\mathrm{L}_{2:2}$ in two dimensions and $\mathrm{L}_{2:0:2}$ in three dimensions; these are spatial harmonics of $\mathrm{L}_{1:1}$ and $\mathrm{L}_{1:0:1}$. They are unstable in the full space, but stable in the $\mathcal{C}$-invariant subspace in which they were computed. All these limit cycles have the same frequency, $0.5\omega_f$.

https://doi.org/10.1017/jfm.2020.543 Published online by Cambridge University Press

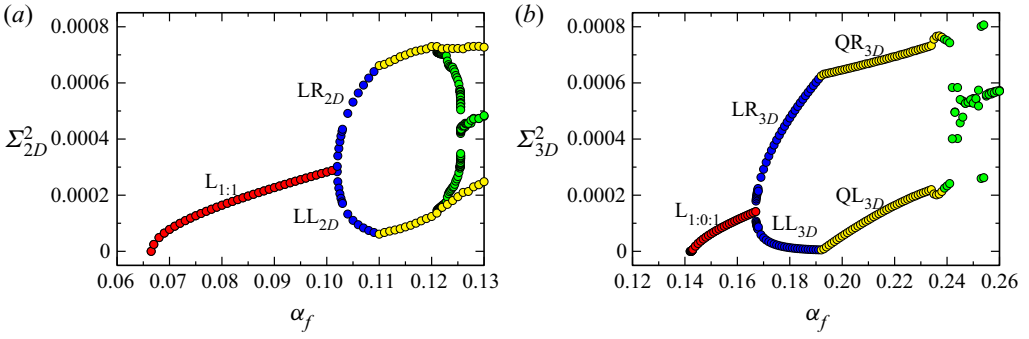


FIGURE 2. Bifurcation diagrams at $Rn = 2 \times 10^4$, $Pr = 1$ and $\omega_f = 1.41$ for (a) the 2-D study and (b) the 3-D study with $\gamma = 0.4$. In both panels, the primary subharmonic limit cycles are denoted in red, the symmetric-conjugate limit cycles in blue, quasi-periodic states of two or three frequencies in yellow, and a myriad of complex states, including chaos, in green.

Figure 4 shows a 3-D perspective of the same 3-D states from figure 3 (supplementary movie 1, available at https://doi.org/10.1017/jfm.2020.543, animates the four limit cycles over two forcing periods). The temperature deviation is maximal a half-forcing-period (a quarter period of the subharmonic response) after the maximal response in the spanwise vorticity. When the magnitude of vorticity (which is pointing almost entirely in the spanwise direction) is small in the interior, the $Q_N = 0.04$ isosurface retracts to the boundary layer regions where dissipative effects dominate.

So far, we have found direct, albeit qualitative, correspondence between the response flows in two and three dimensions. Further increasing α_f beyond $\alpha_f \approx 0.110$ in two dimensions and $\alpha_f \approx 0.193$ in three dimensions, LL and LR (and their conjugates $\mathcal{P}_\tau$LL and $\mathcal{P}_\tau$LR) lose stability via a Neimark–Sacker bifurcation. Following the Neimark–Sacker bifurcation, a pair of symmetrically related quasi-periodic solutions QL_{3D} and QR_{3D} (along with their $\mathcal{P}_\tau$ conjugates) are spawned. These quasi-periodic solutions are characterized by two frequencies and exist on 2-tori in phase space. The first frequency is inherited from the progenitor subharmonic limit cycles (LL_{3D} and LR_{3D}), while the second frequency is lower and corresponds to slow drifts to and from the $L_{2:0:2}$ saddle limit cycle. Supplementary movie 2 shows an animation of the Q_N-criterion at isolevel $Q_N = 0.04$ of QR_{3D} at $\alpha = 0.234$ strobed every two forcing periods at forcing phase π over 176 forcing periods. This movie illustrates the slow drift in the QR_{3D} heteroclinic dynamics between the saddle states $L_{1:0:1}$, LR_{3D} and $L_{2:0:2}$.

Increasing α_f beyond 0.234, QL_{3D} and QR_{3D} (along with their $\mathcal{P}_\tau$ conjugates) undergo a period-doubling cascade. Strobing the phase portrait of the flow every two forcing periods, the period doubling is illustrated for several α_f in figure 5. The last computed QR_{3D} prior to period doubling is illustrated at $\alpha_f = 0.234$; the strobed phase portrait is a single-loop cycle corresponding to the low frequency in the quasi-periodic QR_{3D}. Quasi-statically increasing the forcing amplitude to $\alpha_f = 0.235$, the low frequency is observed to halve (period double) as the strobe map now consists of a two-loop cycle. The period-doubling sequence continues: by $\alpha_f = 0.238$ the strobe map cycle has four loops and 16 loops at $\alpha_f = 0.239$. Increasing α_f further reveals the classic period-doubling route to chaos, culminating at $\alpha_f \approx 0.247$ where the $\mathcal{K}_x\mathcal{K}_z$ symmetry is broken. The spanwise $\mathcal{K}_y$ symmetry is preserved throughout this cascade.

https://doi.org/10.1017/jfm.2020.543 Published online by Cambridge University Press

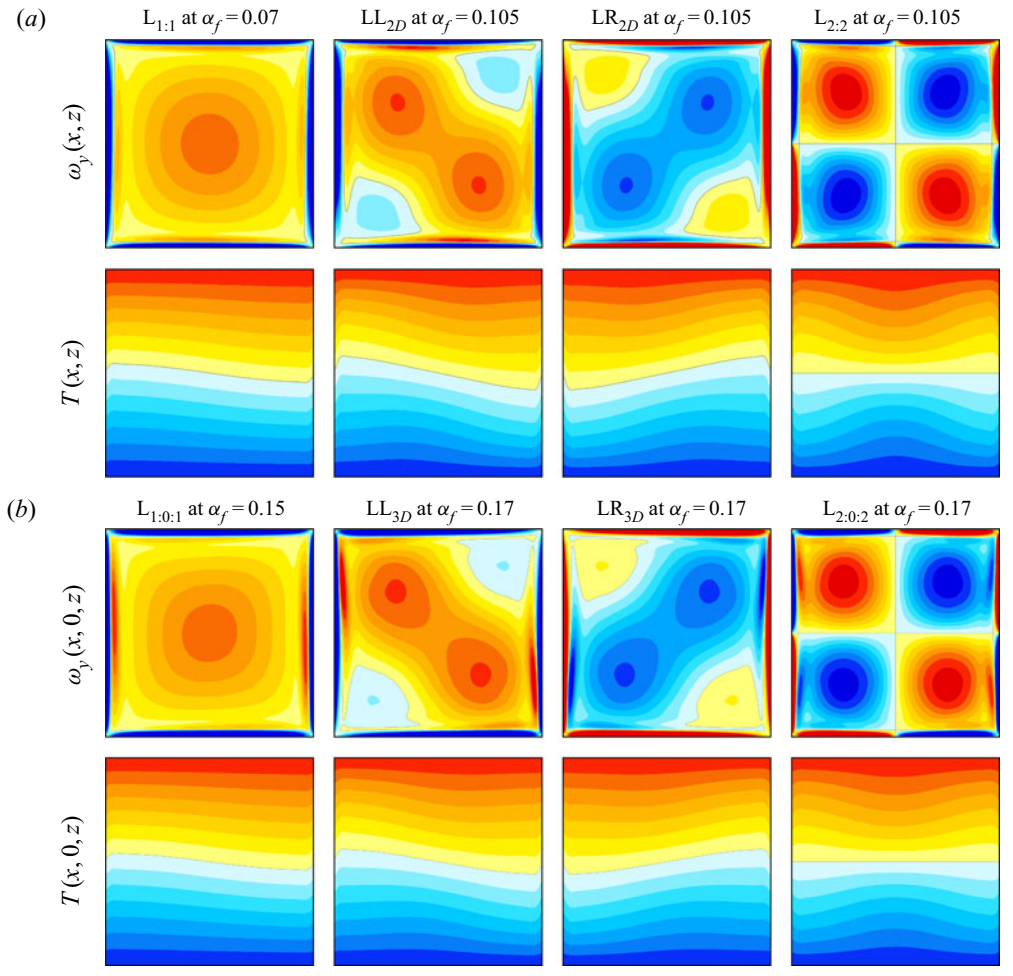


FIGURE 3. Snapshots of subharmonic limit cycle response flows for $Rn = 2 \times 10^4$, $Pr = 1$ and forcing frequency $\omega_f = 1.41$ at forcing amplitude α_f as indicated: (*a*) spanwise vorticity ω_y and isotherms of 2-D flows from Yalim *et al.* (2019*b*); (*b*) ω_y and the isotherms of 3-D flows in the spanwise midplane $y = 0$, but at different α_f as indicated. The isotherms and ω_y are shown a half-forcing-period apart.

The symmetry-broken QL_{3D} and QR_{3D} states at $\alpha_f \approx 0.247$ undergo intermittent drifts to and from the $\mathcal{K}_x\mathcal{K}_z$-symmetry subspace. On increasing α_f, the drifts away from the $\mathcal{K}_x\mathcal{K}_z$-symmetry subspace increase in intensity and duration, resulting in the flow momentarily visiting a sloshing state whose dynamics are reminiscent of the dynamics of the 3-tori observed in the 2-D case (Yalim *et al.* 2019*b*).

One of the main findings in Yalim *et al.* (2019*b*) was the unravelling of the gluing bifurcations of the 2-D left- and right-handed quasi-periodic flows into a single symmetric quasi-periodic flow. Such dynamics are also observed here in three dimensions for $\alpha_f \geq 0.247$. An example of a glued solution at $\alpha_f = 0.26$ is shown in figure 6, which includes a strobed (every two forcing periods) phase portrait of the flow along with a selection of flow snapshots. This glued state is $\mathcal{K}_x\mathcal{K}_z$ symmetric and experiences heteroclinic dynamics between the saddle states $L_{1:0:1}$, LL_{3D}, LR_{3D} and $L_{2:0:2}$ (snapshots of the flow near these

https://doi.org/10.1017/jfm.2020.543 Published online by Cambridge University Press

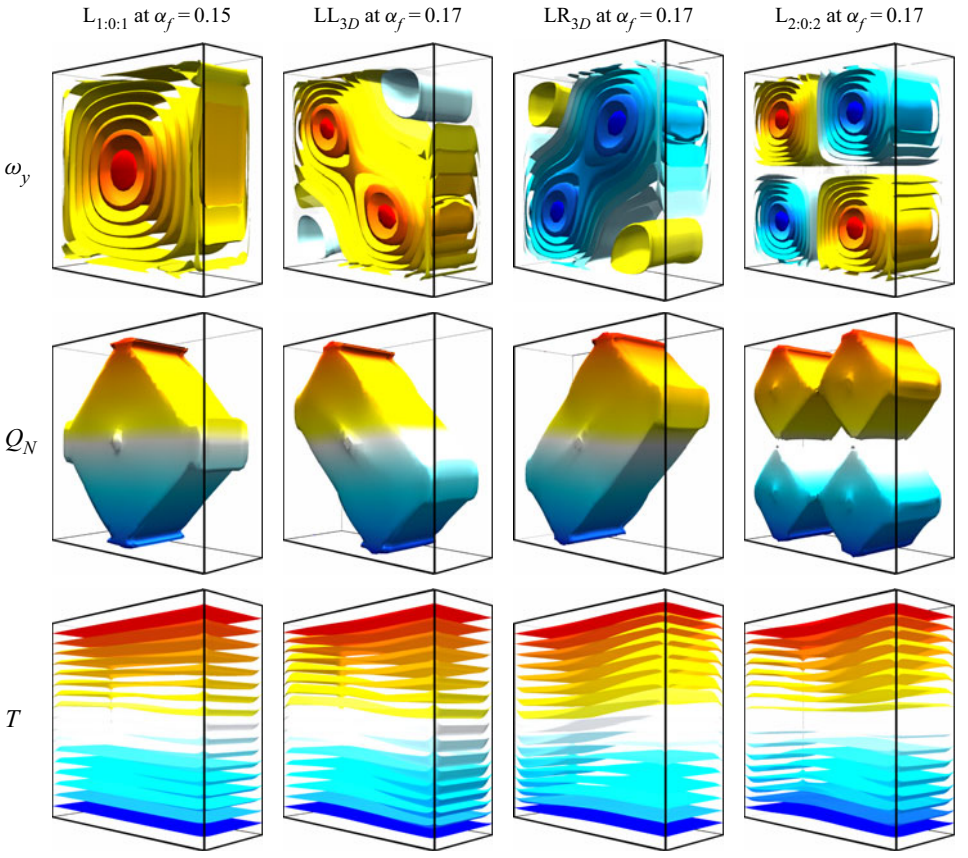


FIGURE 4. Snapshots of subharmonic limit cycle response flows for $Rn = 2 \times 10^4$, $Pr = 1$ and forcing frequency $\omega_f = 1.41$ at forcing amplitude α_f as indicated. The spanwise vorticity ω_y and the normalized Q-criterion Q_N are shown a half-forcing-period behind the isotherms T. The T value is used to colour the $Q_N = 0.04$ isosurface. Supplementary movie 1 provides an animation over two forcing periods.

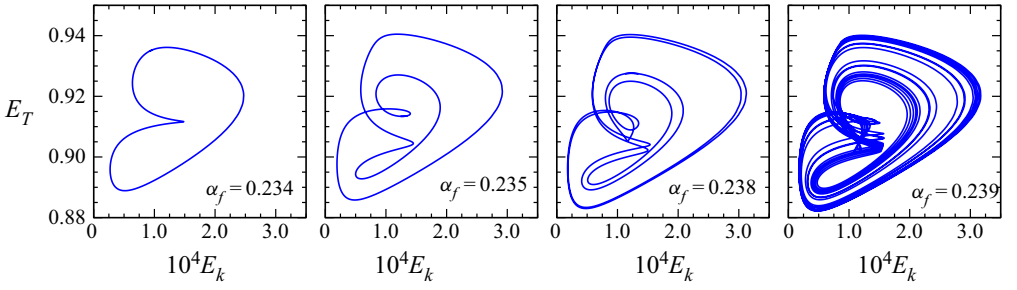


FIGURE 5. Strobe maps (every two forcing periods at forcing phase 0) of QR_{3D} using the kinetic energy $E_k = 0.5 \iiint_V \boldsymbol{u}^2 \, \mathrm{d}V$ and global temperature measure $E_T = 30 \iiint_V T^2 \, \mathrm{d}V$ at $\omega_f = 1.41$ and α_f as indicated. Supplementary movie 2 animates the $\alpha_f = 0.234$ case.

https://doi.org/10.1017/jfm.2020.543 Published online by Cambridge University Press

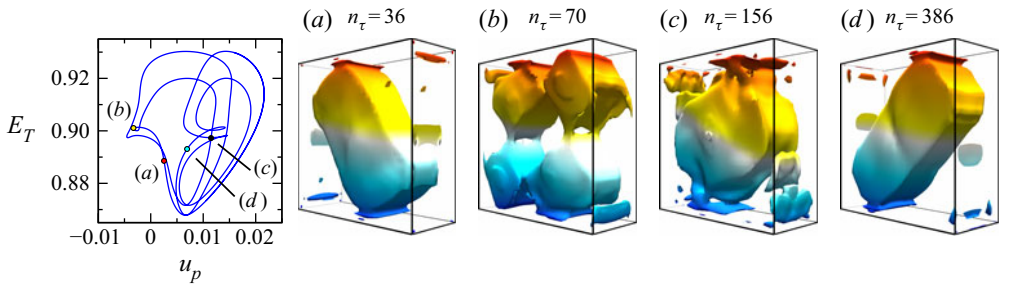


FIGURE 6. Strobe map (every two forcing periods at phase 0) of QR_{3D} using $u_p = u(1/\sqrt{8}, 0, 1/\sqrt{8}, t)$ and E_T at $\omega_f = 1.41$ and $\alpha_f = 0.26$. The snapshots of isosurface $Q_N = 0.04$ at the various forcing periods indicated are shown as coloured symbols in the strobed phase portrait. A strobed animation over 688 forcing periods is shown in supplementary movie 3.

states are shown in figure 6). Supplementary movie 3 animates the strobed flow over 688 forcing periods. The complex gluing bifurcations are described in Yalim *et al.* (2019*b*) for the 2-D parametrically forced flow, and here we have shown they persist in three dimensions.

For $\alpha_f > 0.26$, the flow becomes increasingly complicated, with higher harmonics such as $L_{3:0:3}$ being observed transiently. This was also the case in the experiments of Benielli & Sommeria (1998) as they increased the forcing amplitude. Such flows require substantially increased resolution, in both space and time.

4. Wave breaking

The 3-D response flows described earlier were all driven at $\omega_f = 1.41 \approx 2\sigma_{1:0:1}$, and even at the largest forcing amplitudes considered they remained quasi-2-D with spanwise variation only found in their boundary layers and globally being spanwise $\mathcal{K}_y$ invariant. In this section, we consider a forcing detuned away from the primary subharmonic modal response, corresponding to $\omega_f = 1.34$ and forcing amplitude $\alpha_f = 0.3$. This is motivated by the 2-D study in Yalim *et al.* (2017), where the response flow was observed to undergo violent wave breaking when forced at a frequency a little lower than that of the primary subharmonic mode and forced at a relative high amplitude. Likewise, the experiments of Benielli & Sommeria (1998) observed secondary instability and wave breaking in this regime.

The simulation with $\omega_f = 1.34$ and $\alpha_f = 0.3$ was initiated with a spatially uniformly distributed perturbation with zero mean and small variance from the static linearly stratified state. The parametrically excited subharmonic $L_{1:0:1}$ mode undergoes exponential growth in its kinetic energy over approximately 10^3 forcing periods, at which time it reaches saturation. During the initial 10^3 forcing periods, the isotherms remain essentially spanwise invariant, much like those shown in figure 4 at lower $\alpha_f \sim 0.17$. Following this initial growth phase, the flow begins to slosh back and forth about the spanwise y axis. One salient feature of the isotherms in this regime is their large deviation away from being horizontal. In the previous section, the deviation away from horizontal isotherms was small. In contrast, in this wave-breaking regime, the zero-level isotherm is advected approximately one-third of the way up and down the $x = \pm 0.5$ sidewalls, while isotherms closer to the top and bottom endwalls have strong violent interactions with the same sidewalls, reminiscent of splashing. Together with these splashing events,

https://doi.org/10.1017/jfm.2020.543 Published online by Cambridge University Press

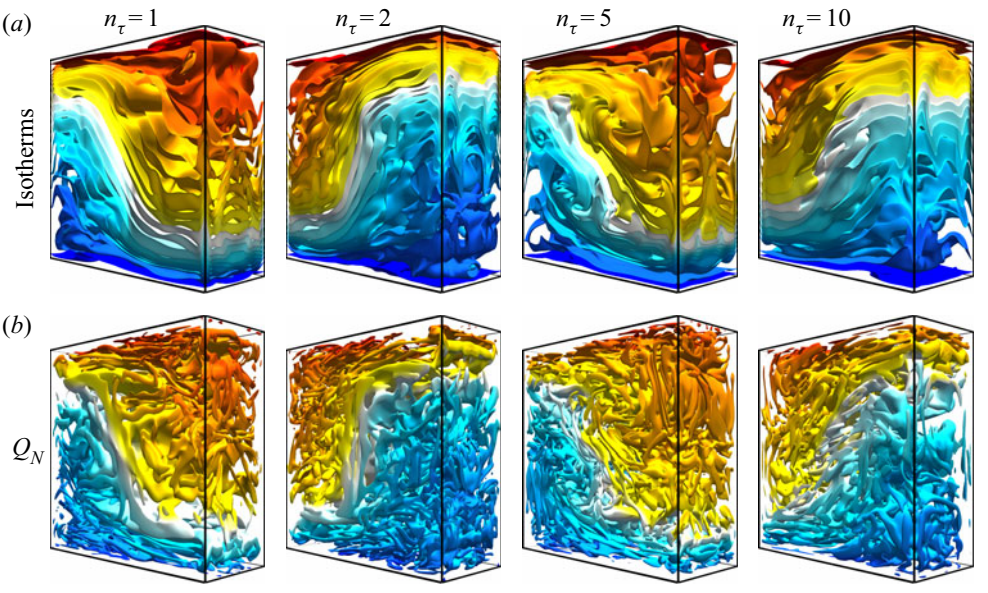


FIGURE 7. Snapshots of isotherms (a) and Q_N-criterion at isolevel $Q_N = 0.04$ coloured by the temperature (b) at forcing periods $n_\tau = 1, 2, 5$ and 10 covering a transient wave-breaking event, with forcing frequency $\omega_f = 1.34$ and forcing amplitude $\alpha_f = 0.3$. Supplementary movies 4 and 5 animate these over 10 forcing periods.

there are separations in the boundary layers and the formation of lambda and hairpin vortices. Also in the interior, the sloshing results in overturning in the isotherm and a violent wave-breaking event leading to the production of fine-scale intense 3-D structures in the interior. All these structures are illustrated in supplementary movies 4–6 which animate the isotherms and Q_N-criterion over the 10 forcing periods corresponding to this wave-breaking event. Snapshots from these movies at forcing periods $n_\tau = 1, 2, 5$ and 10 are shown in figures 7 and 8. The views in figure 7 and supplementary movies 4 and 5 show 3-D perspectives of the isotherms and the $Q_N = 0.04$ isosurface (coloured by T), whereas figure 8 and supplementary movie 6 are contour plots of T and Q_N in the three midplanes $x = 0$, $y = 0$ and $z = 0$.

The snapshots in figures 7 and 8 show a range of small- and large-scale structures in the cavity. These are correlated with hairpin and lambda vortices spawned near the boundary. In the interior, there are also temperature inversions due to the sloshing motion that vary in intensity over the 10 forcing periods and lead to small-scale vortical structures. The localized vortical regions are identified by $Q_N > 0$ (shown in red), while localized shear regions are identified by $Q_N < 0$ (shown in blue) and are correlated with strong gradients in T. At $n_\tau = 1$, the flow is spanwise reflection symmetric $\mathcal{K}_y$ and invariant to the combined x and z reflection symmetries $\mathcal{K}_x\mathcal{K}_z$. By $n_\tau \approx 5$, the interior is undergoing wave breaking and all the spatial symmetries have been broken. The broken symmetries are more pronounced in the snapshots at $n_\tau = 10$. Symmetry breaking implies the existence of conjugate states, and their presence may lead to heteroclinic dynamics with excursions to and from the various states. This may be at play in the wave-breaking regime. In Yalim *et al.* (2017), wave breaking was investigated using 2-D simulations over tens of thousands of forcing periods, and intermittent excursions between various states that are typical of heteroclinic dynamics were observed. The time scales involved in heteroclinic dynamics

https://doi.org/10.1017/jfm.2020.543 Published online by Cambridge University Press

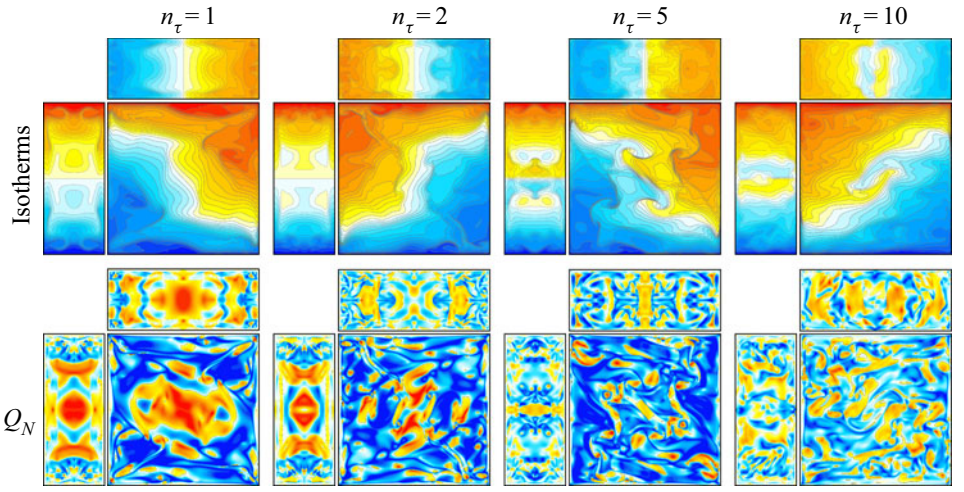


FIGURE 8. Snapshots of the isotherms and Q_N-criterion along the various vertical and horizontal midplanes at the times indicated during a transient wave-breaking event at $\omega_f = 1.34$ and $\alpha_f = 0.3$. Each panel consists of the square vertical $y = 0$ midplane, with the horizontal $z = 0$ midplane above it, and the vertical $x = 0$ midplane to its left. Supplementary movie 6 shows an animation over 10 forcing periods.

make a detailed investigation in three dimensions prohibitively expensive. Furthermore, wave breaking in three dimensions is qualitatively different from wave breaking in two dimensions; three dimensions involves intense temperature gradients in the spanwise direction, which are absent in the 2-D idealization, and these are necessary for the baroclinic production of the intense tube-like vortex structures that are clearly evident throughout the container in figure 7. In two dimensions, the vorticity only has a single component, resulting in spanwise-invariant vortex sheets.

5. Conclusions

We set out to determine the extent to which the 2-D results (Yalim *et al.* 2019*b*) persist in three dimensions. Using the same geometry and protocol as in the experiments of Benielli & Sommeria (1998) to explore the response flow for a forcing frequency corresponding to the primary subharmonic modal response, and the *Rn* used in two dimensions, we established excellent qualitative correspondence between the 2-D and 3-D results, capturing the complex dynamics from onset of the subharmonic response through the various symmetry-breaking and complex heteroclinic bifurcations, including gluing bifurcations and heteroclinic period-doubling bifurcations as the forcing amplitude is increased. The correspondence is not quantitative primarily because the forcing amplitude at which these dynamics manifest is larger in three dimensions than in two dimensions. Large forcing amplitudes are needed to overcome the added viscous damping in the spanwise sidewall boundary layers in three dimensions. In the *Rn* regime considered, the amplitude needed in three dimensions is very roughly twice that needed in two dimensions. The qualitative correspondence between two and three dimensions was established up to forcing amplitude $\alpha_f \approx 0.26$.

https://doi.org/10.1017/jfm.2020.543 Published online by Cambridge University Press

Establishing a correspondence between two and three dimensions is important because, even in this simplified geometric setting, parametrically forced stratified flows in the low-dissipation regime (large Rn) have very rich and complicated dynamics. To explore this dynamics in three dimensions is currently prohibitively expensive, but quite do-able in two dimensions. Keeping everything else the same, switching from a 2-D to a 3-D simulation increases the cost by a factor at least equal to the number of collocation points in the third direction. At the $Rn = 2 \times 10^4$ used in this study, the 3-D simulations in regimes where the response flow was quasi-2-D needed 49^3 collocation points in space and up to 200 time steps per period. When the response flow is fully 3-D rather than quasi-2-D, the computational requirements to resolve the flow grow enormously. In the example studied here, where the forcing frequency was reduced from $\omega_f = 1.41$ to 1.34 and the forcing amplitude was increased to $\alpha_f = 0.30$, keeping the same Rn, spatial resolution had to be increased to 385^3 and the time steps per period increased to 4000. The increase in the cost of computing a single forcing period of a fully 3-D case compared to the quasi-2-D case is roughly $(385/49)^3 \times (4000/200) \approx 10^4$.

In comparing 3-D and 2-D responses, we introduced a normalized Q-criterion, Q_N, which takes some of the guesswork out of selecting which Q isolevel to visualize. This has a tighter connection with the standard Q-criterion used to identify regions of space dominated by vortex structures than the Ω-criterion. Its relation to the Q-criterion is akin to the relationship between correlation and covariance in statistics; both correlation and Q_N varying in $[-1, 1]$. The Q_N-criterion provides a simple visualization of the transition from quasi-2-D dynamics to fully 3-D responses.

In Yalim *et al.* (2019*a*), a small number of 2-D simulations were used to calibrate a reduced model for the critical curve, where the linearly stratified base state becomes unstable. This model is based on a modal approximation of viscous effects that bypasses complications due to the non-commutativity of spatial differentiation operators resulting from confinement and the imposition of associated boundary conditions. Such a modal reduction can in theory be extended to the 3-D case, with a small number of 3-D simulations determining fitting parameters, and facilitate the determination of where in (ω_f, α_f) parameter space specific modes are excited, an undertaking that would be prohibitively expensive to do via 3-D simulations or even Floquet analysis. This could also lead to a better understanding of the transition to fully 3-D, complicated responses in terms of triadic resonances, as anticipated by McEwan (1971) and McEwan, Mander & Smith (1972).

Acknowledgements

We thank ASU Research Computing facilities and the NSF XSEDE programme for providing compute resources, and K. Wu for the original code.

Declaration of interests

The authors report no conflict of interest.

Supplementary movies

Supplementary movies are available at https://doi.org/10.1017/jfm.2020.543.

https://doi.org/10.1017/jfm.2020.543 Published online by Cambridge University Press

References

BENIELLI, D. & SOMMERIA, J. 1998 Excitation and breaking of internal gravity waves by parametric instability. *J. Fluid Mech.* **374**, 117–144.

BOURUET-AUBERTOT, P., SOMMERIA, J. & STAQUET, C. 1995 Breaking of standing internal gravity waves through two-dimensional instabilities. *J. Fluid Mech.* **285**, 265–301.

DAUXOIS, T., JOUBAUD, S., ODIER, P. & VENAILLE, A. 2018 Instabilities of internal gravity wave beams. *Annu. Rev. Fluid Mech.* **50**, 1–28.

HUNT, J. C., WRAY, A. A. & MOIN, P. 1988 Eddies, streams, and convergence zones in turbulent flows. In *Proceedings of the Summer Program*, pp. 193–208. Center for Turbulence Research.

JOUBAUD, S., MUNROE, J., ODIER, P. & DAUXOIS, T. 2012 Experimental parametric subharmonic instability in stratified fluids. *Phys. Fluids* **24**, 041703.

LIU, C., WANG, Y., TANG, Y. & DUAN, Z. 2016 New omega vortex identification method. *Sci. China Phys. Mech. Astron.* **59**, 684711.

LOPEZ, J. M., WELFERT, B. D., WU, K. & YALIM, J. 2017 Transition to complex dynamics in the cubic lid-driven cavity. *Phys. Rev. Fluids* **2**, 074401.

MCEWAN, A. D. 1971 Degeneration of resonantly-excited standing internal gravity waves. *J. Fluid Mech.* **50**, 431–448.

MCEWAN, A. D., MANDER, D. W. & SMITH, R. K. 1972 Forced resonant second-order interaction between damped internal waves. *J. Fluid Mech.* **55**, 589–608.

MCEWAN, A. D. & ROBINSON, R. M. 1975 Parametric instability of internal gravity waves. *J. Fluid Mech.* **67**, 667–687.

MERCADER, I., BATISTE, O. & ALONSO, A. 2010 An efficient spectral code for incompressible flows in cylindrical geometries. *Comput. Fluids* **39**, 215–224.

STAQUET, C. & SOMMERIA, J. 2002 Internal gravity waves: from instabilities to turbulence. *Annu. Rev. Fluid Mech.* **34**, 559–593.

SUTHERLAND, B. R. 2013 The wave instability pathway to turbulence. *J. Fluid Mech.* **724**, 1–4.

THORPE, S. A. 1968 On standing internal gravity waves of finite amplitude. *J. Fluid Mech.* **32**, 489–528.

WU, K., WELFERT, B. D. & LOPEZ, J. M. 2018 Complex dynamics in a stratified lid-driven square cavity flow. *J. Fluid Mech.* **855**, 43–66.

YALIM, J., LOPEZ, J. M. & WELFERT, B. D. 2018 Vertically forced stably stratified cavity flow: instabilities of the basic state. *J. Fluid Mech.* **851**, R6.

YALIM, J., WELFERT, B., LOPEZ, J. & WU, K. 2017 V0066: resonant collapse in a harmonically forced stratified cavity. In *American Physical Society Division of Fluid Dynamics 2017 Gallery of Fluid Motion*, doi:10.1103/APS.DFD.2017.GFM.V0066. American Physical Society.

YALIM, J., WELFERT, B. D. & LOPEZ, J. M. 2019*a* Modal reduction of a parametrically forced confined viscous flow. *Phys. Rev. Fluids* **4**, 103903.

YALIM, J., WELFERT, B. D. & LOPEZ, J. M. 2019*b* Parametrically forced stably stratified cavity flow: complicated nonlinear dynamics near the onset of instability. *J. Fluid Mech.* **871**, 1067–1096.

https://doi.org/10.1017/jfm.2020.543 Published online by Cambridge University Press